ARTICLES
https://doi.org/10.1038/s41929-021-00602-4

nature catalysis

Check for updates

Coordination and activation of nitrous oxide by iron zeolites

Max L. Bols[1,7], Benjamin E. R. Snyder[2,6,7], Hannah M. Rhoda[2], Pieter Cnudde[3], Ghinwa Fayad[4], Robert A. Schoonheydt[1]✉, Veronique Van Speybroeck[3]✉, Edward I. Solomon[2,5]✉ and Bert F. Sels[1]✉

Iron-containing zeolites are heterogeneous catalysts that exhibit remarkable activity in the selective oxidation of inert hydrocarbons and catalytic decomposition of nitrous oxide (N_2O). The reduction of N_2O is critical to both these functions, but experimental data tracking the iron active sites during N_2O binding and activation are limited. Here, the N_2O-ligated Fe(II) active site in iron-exchanged zeolite beta is isolated and characterized by variable-temperature Mössbauer, diffuse reflectance UV-vis-NIR and Fourier transform infrared spectroscopy. N_2O binds through the terminal nitrogen atom with substantial backbonding from the Fe(II) centre at low temperature. At higher temperatures, the Fe-N_2O interaction is weakened, facilitating isomerization to the O-bound form, which is competent in O-atom transfer. Density functional theory calculations show the geometric and electronic structure requirements for N_2O binding and activation. A geometric distortion imposed by the zeolite lattice plays an important role in activating N_2O. This highlights a mechanism for structural control over function in Fe-zeolite catalysts.

Nitrous oxide (N_2O) is a potent and selective oxidant, and also a major cause of stratospheric ozone depletion and the third largest contributor to anthropogenic global warming[1]. It is generated in large quantities as a side product in the production of adipic acid and nitric acid, but it remains under-utilized due to its high kinetic stability. Understanding the binding and activation of N_2O by transition metal catalysts is therefore of notable interest for the use of N_2O as an oxidant, and for its catalytic decomposition to environmentally benign O_2 and N_2. However, the N_2O ligand interacts only weakly both as a σ donor and as a π acceptor. Consequently, only a handful of N_2O-ligated transition metal centres have been successfully isolated and characterized[2–6]. Binding through the terminal nitrogen is generally preferred due to backbonding effects[2]. Iron-exchanged zeolites stabilize an $S=2$ square planar Fe(II) site (α-Fe(II)) that activates N_2O, forming a highly reactive Fe(IV)=O intermediate (α-O) that is active in the low-temperature hydroxylation of inert C–H bonds (for example, methane and benzene)[7,8] and the catalytic decomposition of N_2O[9,10]. Despite the large body of literature on N_2O activation and decomposition by Fe-zeolites, experimental spectroscopic data are limited[11–16], and no studies exist that track the state of the α-Fe(II) active site over the course of N_2O binding and activation. In this Article, N_2O-ligated α-Fe(II) complexes are identified in Fe-exchanged zeolite beta (Fe-*BEA) by diffuse reflectance spectroscopy (DR-UV-vis-NIR), Fourier transform infrared spectroscopy (FTIR) and Mössbauer spectroscopy. The thermodynamics and kinetics of N_2O activation to form α-O are determined with operando DR-UV-vis-NIR spectroscopy. Density functional theory (DFT) models of N_2O-ligated intermediates are evaluated against experimental data and used to interrogate the reaction coordinate for N_2O activation. They demonstrate the role of the ligand field from the zeolite lattice in tuning the thermodynamics and kinetics of N_2O binding and activation.

Results

Spectroscopic identification of a N_2O-bound intermediate. We used room-temperature ^{57}Fe Mössbauer spectroscopy to probe the state of the Fe sites during N_2O binding and activation (Fig. 1a–c). A sample containing >95% ^{57}Fe-enriched α-Fe(II) (Fig. 1a; see Supplementary Fig. 1 for the full velocity range spectrum) was exposed to an atmosphere of 35 vol% N_2O in He at room temperature. Upon exposure to N_2O, the α-Fe(II) signal is no longer present, and a single new component appears with an isomer shift of $\delta = 1.09\,mm\,s^{-1}$ and quadrupole splitting $|\Delta E_Q| = 1.53\,mm\,s^{-1}$ (Fig. 1b), characteristic of high spin ($S=2$) Fe(II). We name this N_2O-ligated high-spin Fe(II) component 'α-N_2O'. After 30 min at 433 K, the α-N_2O is fully converted to α-O, as identified by Mössbauer spectroscopy (Fig. 1c)[8,17,18]. α-N_2O is therefore the Fe(II) precursor to the Fe(IV)=O α-O intermediate.

To further identify α-N_2O, we collected Mössbauer data at various N_2O concentrations (Fig. 1d). The room-temperature Mössbauer spectrum varies continuously between that of α-Fe(II) (low concentration limit) and that of α-N_2O (high concentration limit). Beyond 35 vol% N_2O, the active Fe sites are fully bound and no further spectral changes occur. The signals observed at intermediate N_2O concentrations may result from an equilibrium between α-Fe(II) and α-N_2O that exchanges rapidly relative to the ~10^{-7}-s lifetime of the ^{57m}Fe 14.4-keV nuclear excited state probed by Mössbauer spectroscopy, yielding an averaged signal (Supplementary Note 1)[19]. The fully bound sample (35 vol% N_2O) was chosen to study the temperature dependence of the α-N_2O Mössbauer spectrum (Fig. 1e). With decreasing temperature down to 100 K, both the isomer shift and the

[1]Department of Microbial and Molecular Systems, Centre for Sustainable Chemistry and Engineering, KU Leuven, Leuven, Belgium. [2]Department of Chemistry, Stanford University, Stanford, CA, USA. [3]Centre for Molecular Modelling, Ghent University, Zwijnaarde, Belgium. [4]Laboratoire Catalyse et Spectrochimie, CNRS, ENSICAEN, Université de Caen, Caen, France. [5]Photon Science, SLAC National Accelerator Laboratory, Menlo Park, CA, USA. [6]Present address: Department of Chemistry, University of California Berkeley, Berkeley, CA, USA. [7]These authors contributed equally: Max L. Bols, Benjamin E. R. Snyder. ✉e-mail: robert.schoonheydt@kuleuven.be; veronique.vanspeybroeck@ugent.be; solomone@stanford.edu; bert.sels@kuleuven.be

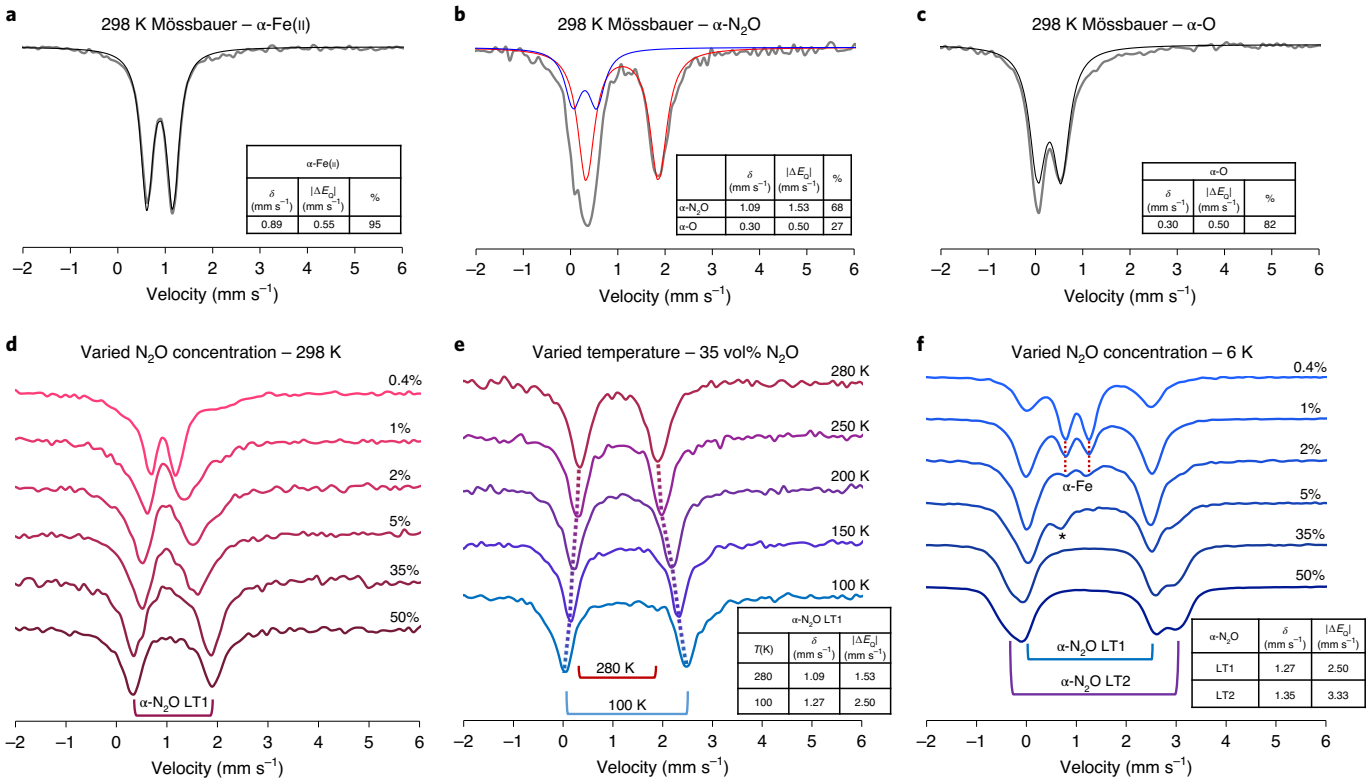

Fig. 1 | Mössbauer spectroscopy on α-N_2O. a–c, Deconvoluted room-temperature Mössbauer spectra with the identified contributions tabulated. In seperate panels the spectra of α-Fe(II) (**a**), α-N_2O (red component; some conversion to α-O is also observed—blue component) (**b**) and α-O formed from heating the sample of α-N_2O to 433 K for 30 min (**c**). **d**, Room-temperature Mössbauer spectra of α-Fe(II) in the presence of atmospheres with increasing percentages of N_2O. The Mössbauer spectra exhibit change until the N_2O atmosphere is ≥35%; further change upon increasing the percentage of N_2O is not observed. **e**, Temperature dependence of the Mössbauer spectra of the 35 vol% N_2O sample. **f**, Low-temperature (6 K) Mössbauer spectra of α-Fe(II) with increasing percentage of N_2O in the atmosphere. These data show the conversion of a mono-N_2O bound (α-N_2O LT1) to a bis-N_2O bound form (α-$(N_2O)_2$ LT2). *Limited conversion to α-O.

quadrupole splitting increase in magnitude. Further cooling to 6 K (Fig. 1f) induces no further increase and the Mössbauer parameters remain at $\delta = 1.27\,mm\,s^{-1}$ and $|\Delta E_Q| = 2.50\,mm\,s^{-1}$. The temperature dependence of the quadrupole splitting ($\Delta|\Delta E_Q| = 0.97\,mm\,s^{-1}$) is characteristic of a temperature-dependent structural change, for example the contraction of metal-ligand bonds at low temperature[20]. Interestingly, at 6 K the Mössbauer spectra (Fig. 1f) show an additional species is present when the atmosphere exceeds 1 vol% N_2O. Together with the DFT calculations presented in Extended Data Fig. 1, this leads us to assign the [$\delta = 1.27\,mm\,s^{-1}$; $|\Delta E_Q| = 2.50\,mm\,s^{-1}$] doublet of α-$N_2O$ to a mono-N_2O bound site, and the [$\delta = 1.35\,mm\,s^{-1}$; $|\Delta E_Q| = 3.33\,mm\,s^{-1}$] doublet to a bis-$N_2O$-bound site, which we name 'α-$(N_2O)_2$ LT2'. The coordination of a third N_2O ligand is not feasible.

Based on the Mössbauer data alone we cannot discriminate between binding modes of N_2O. We therefore collected variable-temperature FTIR spectra at varied N_2O loadings. In the N_2O antisymmetric stretch region, two features appear upon dosing 44 equiv. N_2O per iron at room temperature (Fig. 2a). Only the feature at 2,283 cm^{-1} correlates with the presence of Fe(II). We assign the feature at 2,235 cm^{-1} to lattice-adsorbed N_2O. In the symmetric stretch region (Fig. 2b), a single feature at 1,340 cm^{-1} is correlated with Fe(II). As these samples of Fe-*BEA contained >95% active Fe, we assign these features as the symmetric (ν_s) and antisymmetric (ν_{as}) stretches of the N_2O ligand of α-N_2O. A blueshift of the N_2O symmetric stretch by 55 cm^{-1} relative to gas-phase N_2O ($\nu_s = 1{,}285\,cm^{-1}$)[21] upon binding to α-Fe(II) is characteristic of binding through the N atom[15]. Combined spectroscopic data therefore indicate α-N_2O is a single $S = 2$ Fe(II) species containing an N_2O ligand bound through its terminal nitrogen atom.

At 77 K (Fig. 2c,d), similar vibrational features are observed, and we assign these to the same α-N_2O site with $\nu_{as} = 2{,}287\,cm^{-1}$ and $\nu_s = 1{,}341\,cm^{-1}$. The similarity between the room-temperature and low-temperature frequencies indicates that the N_2O ligand remains N-bound at low temperature. Additional bands appear in the FTIR spectra of N_2O-dosed Fe-*BEA at 2,204, 2,295, 2,310, 2,334 and 2,346 cm^{-1} that are not seen on H-*BEA and therefore correlate with Fe(II) (Fig. 2c and Extended Data Figs. 2 and 3). All of these saturate at low p_{N_2O} with low relative intensity and do not relate to the majority α-Fe(II) site. At high p_{N_2O} and low temperature, the mono-N_2O-bound complex transitioned into a bis-N_2O-bound complex (Fig. 1f). At a threshold p_{N_2O} we similarly see the replacement of the 2,287 and 1,341 cm^{-1} bands by a feature at 2,253 cm^{-1} that may be connected to this bis-N_2O-bound α-$(N_2O)_2$ LT2 site (Extended Data Fig. 3). Full FTIR data and further discussion are presented in Supplementary Note 2.

To understand the nature of the Fe(II)–N_2O interaction in α-N_2O, its 6-K Mössbauer parameters and vibrational features are compared to those calculated from candidate models. Model structures were optimized using periodic DFT to account for the zeolite lattice. To calculate the models' vibrational frequencies and Mössbauer parameters, cluster models were excerpted from the periodically optimized models. The calculations were run at the B3LYP-D3 level of theory, including dispersion to properly account for zeolite/adsorbate interactions[22,23]. Starting from a spectroscopically validated DFT model of α-Fe(II)[8,24,25], two mono-N_2O-bound

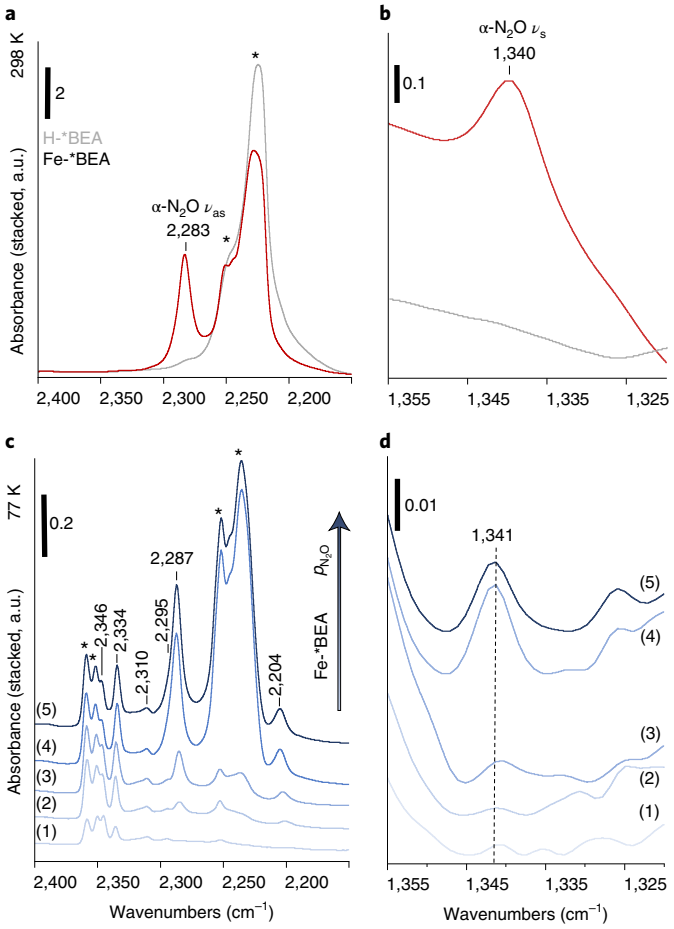

Fig. 2 | Infrared spectroscopy on α-N_2O. a,**b**, Antisymmetric (**a**) and symmetric (**b**) N_2O stretches on H-*BEA and Fe-*BEA respectively exposed to 2.63 and 2.87 mmol N_2O per gram of zeolite at 298 K. **c**,**d**, Antisymmetric (**c**) and symmetric (**d**) N_2O stretches on Fe-*BEA exposed to 0.05, 0.14, 0.28, 0.86 and 2.08 mol N_2O per mol iron at 77 K for spectra 1 to 5, respectively. *Lattice-adsorbed N_2O. All spectra are relative to 550 °C activated H-*BEA or Fe-*BEA.

sites were optimized on the $S=2$ surface, with N_2O bound through either the terminal N atom or terminal O atom. Other binding modes (for example, η^2-O,N) did not yield stable minima. The different distributions of Al within the active site were evaluated using cluster models, and showed limited differences in N_2O binding and activation (Extended Data Fig. 4). The calculated properties of the N- and O-bound models are presented in Fig. 3. Both models accurately model the experimental spectroscopic and thermodynamics parameters, with the N-bound model giving closer agreement. The models confirm the assignment of the 2,287/1,341 cm^{-1} pair of vibrations in FTIR to the antisymmetric and symmetric stretches of η^1-N-bound N_2O on α-Fe(II). In particular, the blueshifted symmetric stretch relative to gas-phase N_2O (experimental[21] $\nu_s=1{,}285\ cm^{-1}$, computed at 1,312 cm^{-1}) is a strong argument for the η^1-N binding mode, both at 298 K and at 77 K. To assess the impact of the zeolite lattice, parallel calculations were performed on cluster models optimized without periodic boundary conditions. The cluster models comprise a double 6MR extended with one T-atom and capped with hydrides. In this case, for large-pore *BEA zeolite, the cluster models give similar results (Extended Data Fig. 1), although the N_2O molecule is located more closely to the six-membered ring due to the absence of the complete zeolite channel environment and the binding enthalpies are more exothermic, especially for the η^1-N model. With larger cluster models the approximation to the periodic calculation results becomes closer still (Extended Data Fig. 6).

Comparing the η^1-O and η^1-N bound models, the 2.13-Å Fe–NNO bond is considerably shorter than the 2.34-Å Fe–ONN bond. This is related to their different calculated electronic structures. For the O-bound intermediate, the Fe–ONN interaction only weakly perturbs the α-Fe(II) electronic structure and the d_{z^2} orbital remains doubly occupied (shown for α-Fe(II) and related to its small $|\Delta E_Q|$ in ref. [8]). In Fe–NNO, on the other hand, the d_{xz} orbital is stabilized by the presence of π backbonding. Compared to the ground state of α-Fe(II), an electron is moved from the d_{z^2} orbital that was lowest in energy and doubly occupied for α-Fe(II) into the d_{xz} orbital, which becomes lowest in energy and doubly occupied for Fe–NNO, resulting in the $(d_{xz})^2(d_{yz})^1(d_{z^2})^1(d_{xy})^1(d_{x^2-y^2})^1$ configuration for the ground state of Fe–NNO. This promotion of a d_{z^2} electron into the $d\pi$ orbital enables π backbonding, and changes the electric field gradient at the ^{57}Fe nucleus, resulting in the larger $|\Delta E_Q|$ (relative to α-Fe(II)). For the O-bound intermediate, the Fe–ONN interaction is weak and the d_{z^2} orbital remains doubly occupied, resulting in the smaller calculated $|\Delta E_Q|$[8,26]. The room-temperature experimental N_2O binding enthalpy of −4.8 kcal mol^{-1} (vide infra) can be correlated with the room-temperature Mössbauer and FTIR spectra (Figs. 1 and 2) with $|\Delta E_Q|=1.53\ mm\ s^{-1}$ and $\nu_{as}=2{,}283\ cm^{-1}$. In cluster model DFT calculations, performed to parallel the periodic calculations, we were able to stabilize an additional local minimum ($\Delta H_{ads,298K}=-3.5$ kcal mol^{-1}) for the N-bound geometry with a longer Fe–N bond length of 2.32 Å with limited backbonding. For this model, $\Delta E_Q=-1.76\ mm\ s^{-1}$ was calculated (Extended Data Fig. 1, η^1-N′ model). The alternative model may correlate to the weakened Fe–N bond for the room-temperature α-N_2O that facilitates isomerization to the O-bound form on the intrinsic reaction coordinate for α-O formation (vide infra).

Thermodynamics of N_2O binding and activation. Site-selective operando DR-UV-vis-NIR spectroscopy was used to derive

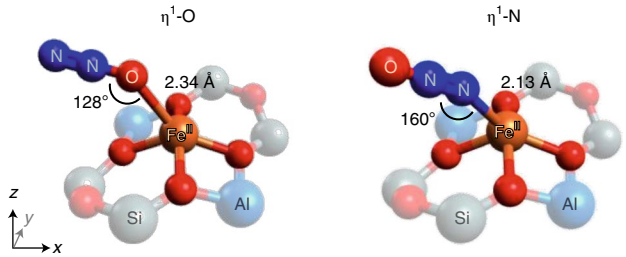

	Experiment	DFT	
	α-N_2O	η^1-O	η^1-N
$\Delta H_{ads,\ 298\ K}$ (kcal mol^{-1})	−4.8	−5.2	−8.3
δ (mm s^{-1})	1.27	0.90	0.92
ΔE_Q (mm s^{-1})	±2.50	+2.06	+2.24
ν_{as} (cm^{-1})	2,287	2,253	2,303
ν_s (cm^{-1})	1,341	1,196	1,324
β-HOMO	–	d_{z^2}	d_{xz}

Fig. 3 | Properties of α-N_2O candidate structures. Comparison of the geometric structures of the η^1-N and η^1-O N_2O-bound models evaluated by periodic DFT. In the table, the calculated spectroscopic parameters of these models are compared to experimental data from α-N_2O collected at 6 K (Mössbauer data) or 77 K (vibrational data). The DFT energies are $\Delta H_{ads,298K}$ values from Extended Data Fig. 5, relative to lattice-bound N_2O. The experimental energy comes from the Van 't Hoff plot in Fig. 4d.

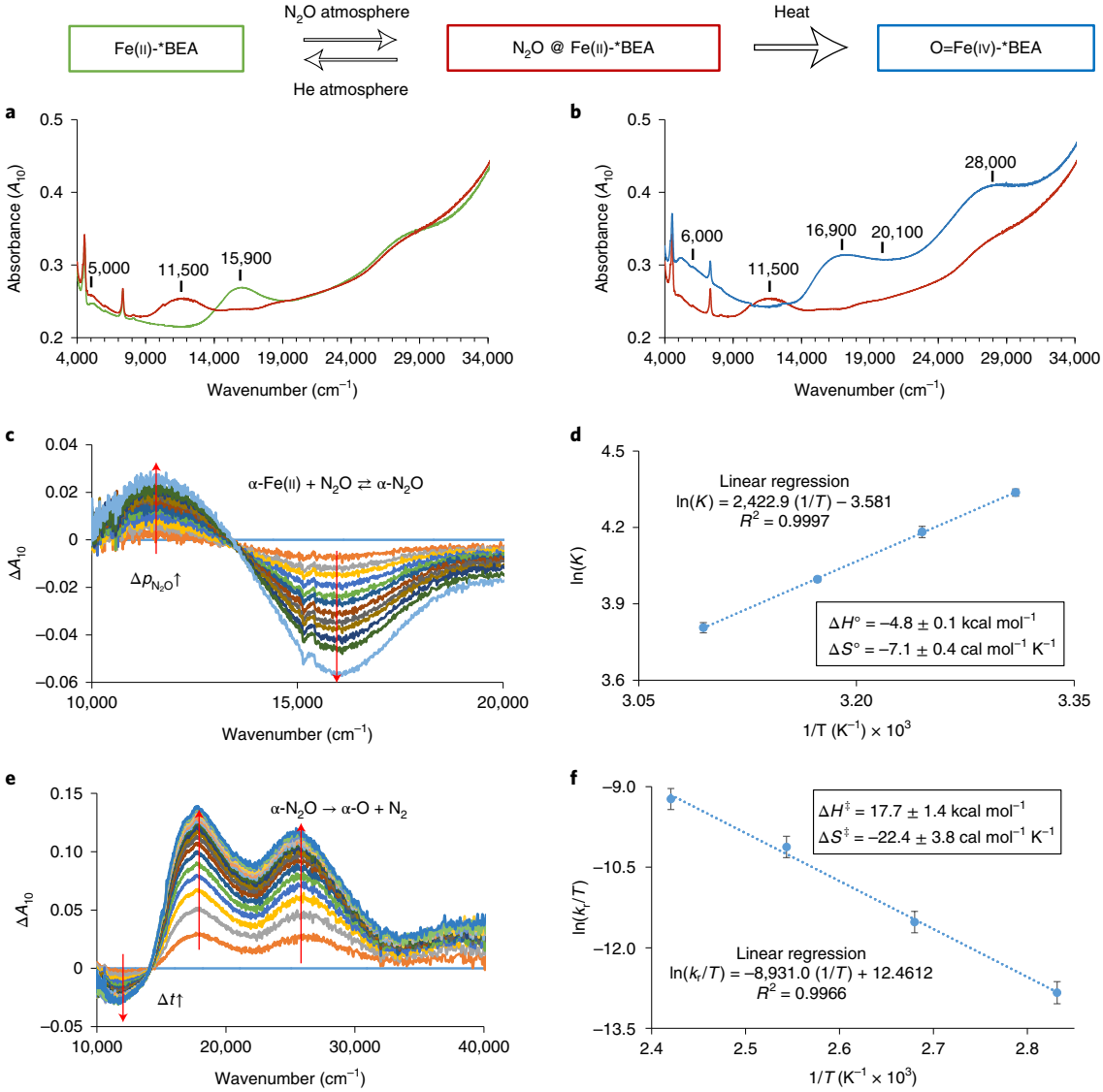

Fig. 4 | UV-vis-NIR spectroscopy of α-N_2O and its thermodynamics. a, Comparison of the DR-UV-vis-NIR spectra of Fe(II)-*BEA before (green) and after (red) introduction of a 35 vol% N_2O in He atmosphere at room temperature. **b**, Comparison of DR-UV-vis-NIR spectra collected before (red) and after (blue) heating at 433 K in a 35 vol% N_2O in He atmosphere for 30 min. **c**, Operando UV-vis difference spectra of Fe-*BEA at 308 K after high-temperature He treatment with p_{N_2O} ranging from 0 to 0.05 atm, showing the equilibrium between α-Fe(II) and α-N_2O. **d**, Van 't Hoff plot of data derived from the adsorption data from operando UV-vis spectra analogous to those shown in Fig. 4c. **e**, Operando UV-vis difference spectra of Fe-*BEA at 373 K following the transformation of α-N_2O to α-O over a time interval of 15 min in an atmosphere of 35 vol% N_2O in He. **f**, Eyring plot of data derived from operando UV-vis spectra analogous to those shown in Fig. 4e. Error bars in Fig. 4d,f indicate the 95% confidence interval of the ordinary least-squares regressions shown in the Supplementary Methods.

the enthalpy and entropy of N_2O binding to α-Fe(II) and of the transition state to α-O. The DR-UV-vis-NIR spectrum of α-Fe(II) is characterized by a 15,900 cm^{-1} ligand field band (Fig. 4a, green spectrum)[8]. On exposing the sample to an atmosphere of 35 vol% N_2O in He at room temperature, the 15,900 cm^{-1} absorption band is lost and a new absorption band appears at 11,500 cm^{-1}, along with a weak absorption feature at 5,000 cm^{-1} (Fig. 4a, red trace). Reverting the atmosphere to 100 vol% He restores the α-Fe(II) spectrum (Extended Data Fig. 7). The new absorption features can be assigned to the α-N_2O intermediate identified by Mössbauer spectroscopy and are in agreement with DFT cluster models (Extended Data Fig. 1). After 30 min at 433 K, the 11,500 cm^{-1} absorption band is lost and absorption bands at 6,000 cm^{-1}, 16,900 cm^{-1}, 20,100 cm^{-1} and 28,000 cm^{-1} appear (Fig. 4b), consistent with the DR-UV-vis-NIR spectrum of α-O[8]. In Supplementary Note 3 we show the analagous trends for α-O sites defined in Fe-*BEA and the α-O sites defined in Fe-ZSM-5 by other authors[7,27,28].

The thermodynamics of N_2O binding to α-Fe(II) was evaluated by the dependence of the equilibrium ratio of the 15,900 cm^{-1} and 11,500 cm^{-1} absorption bands at different p_{N_2O} and temperatures (Fig. 4c). The α-Fe(II) band gradually disappears with increasing p_{N_2O}, whereas the α-N_2O band gradually gains intensity and the presence of an isosbestic point at 13,500 cm^{-1} indicates the interchange between single species. The results were evaluated using the Langmuir adsorption model and the Van 't Hoff equation (Supplementary Methods). The Van 't Hoff plot (Fig. 4d) yields an enthalpy of adsorption of $\Delta H° = -4.8 \pm 0.1$ kcal mol^{-1} and an entropy of adsorption of $\Delta S° = -7.1 \pm 0.4$ cal mol^{-1} K^{-1}. In ref. [29], an experimental $\Delta H° = -12.7 \pm 0.5$ kcal was obtained. However, this

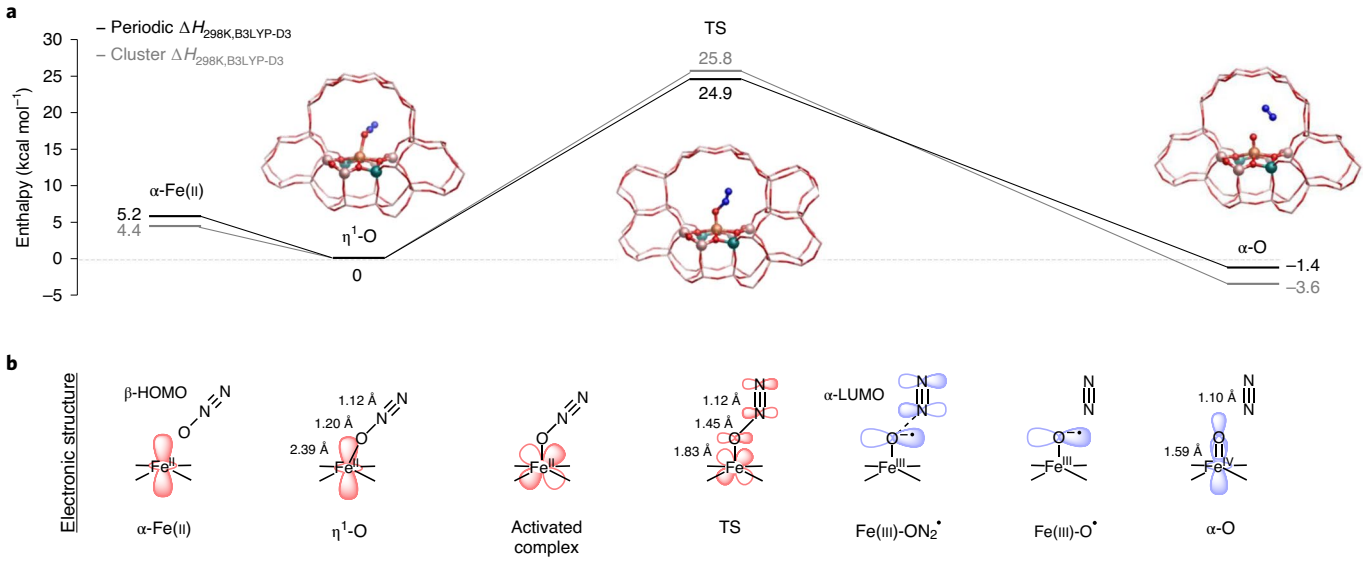

Fig. 5 | Comparison of reaction profiles for N–O cleavage and schematics of the HOMO–LUMO orbitals. a, Reaction profiles calculated with periodic models (black) or with cluster models (grey), both on the $S=2$ surface and using the B3LYP-D3 functional. The reaction starts from unbound N_2O in a van der Waals complex with the zeolite lattice and ends with α-O and liberated N_2. **b**, The evolution of the β-HOMO (highest occupied molecular orbital) leading up to the first electron transfer (red orbitals) is shown schematically, along with the evolution of the α-LUMO reflecting transfer of the second electron after the barrier (blue orbitals). The bond distances are taken from the cluster models.

study was on Fe-ZSM-5 and did not directly observe the adsorption of N_2O onto α-Fe(II).

Next, the transformation of the α-N_2O adsorption complex into α-O was followed by operando UV-vis-NIR spectroscopy at different temperatures. The gradual disappearance of the 11,500 cm^{-1} absorption band coincides with the growth of absorption bands at 16,900 cm^{-1} and 28,000 cm^{-1}, with an isosbestic point at 14,000 cm^{-1} (Fig. 4e). The reaction therefore converts α-N_2O selectively into α-O.

The microkinetics are described by:

$$\alpha - \mathrm{Fe\,(II)} + \mathrm{N_2O_{(g)}} \rightleftarrows \alpha - \mathrm{N_2O} \quad (1)$$

$$\alpha - \mathrm{N_2O} \xrightarrow{k_r} \alpha - \mathrm{O} + \mathrm{N_{2(g)}} \quad (2)$$

and the following parameters are defined, assuming a first-order reaction (2):

$$\text{N$_2$O adsorption equilibrium} \quad K = \frac{k_a}{k_d} = \frac{[\alpha - \mathrm{N_2O}]}{p_{\mathrm{N_2O}}[\alpha - \mathrm{Fe}]} \quad (3)$$

$$\text{Activation of N$_2$O} \quad \frac{\mathrm{d}[\alpha - \mathrm{O}]}{\mathrm{d}t} = k_r[\alpha - \mathrm{N_2O}] \quad (4)$$

$$\text{Rate equation} \quad \frac{\mathrm{d}[\alpha - \mathrm{O}]}{\mathrm{d}t} = \frac{k_r K}{K p_{\mathrm{N_2O}} + 1} p_{\mathrm{N_2O}} \left([\alpha - \mathrm{Fe}]_0 - [\alpha - \mathrm{O}]\right) \quad (5)$$

From the Eyring plot in Fig. 4f, the enthalpy and entropy of the transition state (TS) are $\Delta H^{\ddagger} = 17.7 \pm 1.4$ kcal mol^{-1} and $\Delta S^{\ddagger} = -22.4 \pm 3.8$ cal mol^{-1} K^{-1} (calculation details are provided in the Supplementary Methods). The resulting apparent activation energy is 12.8 ± 1.5 kcal mol^{-1}. On Fe-ZSM-5, experimental values for the apparent activation energy of 10 kcal mol^{-1}, 15 kcal mol^{-1} and 16.7 kcal mol^{-1} have been reported[7,29,30], but these values were inferred indirectly without site-selective monitoring of the active α-Fe(II) site.

Computational evaluation of N_2O activation. Periodic calculations with the B3LYP-D3 functional were performed to evaluate N_2O binding and activation by α-Fe(II). As recent studies highlight the potential importance of electrostatic confinement effects on the metallozeolite reactivity[22,31], the periodic calculations were compared to parallel cluster model calculations to assess how confinement of the reactants in the *BEA pore affects the barrier to O-atom transfer. Additional detail on this is presented in the Supplementary Methods. As reference level for the calculations, N_2O adsorbed as a van der Waals complex in the zeolite lattice (that is, away from the Fe active site) was used (Extended Data Fig. 5). The N_2O binding enthalpies are more exothermic in the periodic models than in the cluster models, especially in the N-bound case (compare Extended Data Figs. 1 and 5). Periodic models, or larger cluster models (Extended Data Fig. 6), are therefore required to accurately model van der Waals interactions between the lattice and the N_2O ligand.

The reaction coordinate for O-atom transfer was calculated using both periodic and cluster models, with reasonable agreement (Fig. 5). The first step is N_2O binding to α-Fe(II). Only the O-bound intermediate can participate in O-atom transfer to Fe(II). Periodic calculations predict a binding enthalpy of $\Delta H_{ads,298K} = -5.2$ kcal mol^{-1} for the O-bound intermediate. Proceeding from the O-bound intermediate, the Fe–ONN bond begins to contract and becomes collinear with the molecular z axis, causing the β (spin down) electron on Fe(II) to be transferred from the d_{z^2} orbital into the βd_{xz} orbital (activated complex in Fig. 5). This enables π back donation from the Fe(II) centre into the empty $\beta\pi^*$ orbital of the N_2O ligand. As the N–O bond elongates, the Fe back donation increases. A transition state for N–O cleavage is found on the $S=2$ surface, with an activation enthalpy of $\Delta H^{\ddagger} \approx 25$ kcal mol^{-1} for both the periodic and cluster models (the $S=1$ transition state is destabilized by an additional 20 kcal mol^{-1}). At the transition state, the N–O bond has elongated to 1.45 Å, the Fe–ONN bond has contracted to 1.83 Å and the N_2O ligand is bent (∠ONN = 138°). These geometric changes correlate to

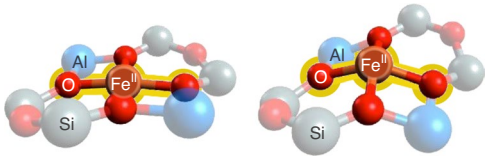

	Unconstrained	BEA
d(Fe–O)$_{avg}$	2.01 Å	1.99 Å
∠O–Fe–O	173°	145°
ΔH_{ads}(η^1-O)	2.7	−4.4
ΔH_{app}	29.1	21.4

Fig. 6 | Correlation of α-Fe(II) geometric structure with function. An unconstrained optimized geometry of α-Fe(II) is compared to one constrained by the BEA lattice. Distortion of the O-Fe-O angle highlighted in yellow promotes N_2O binding and activation. Enthalpies, derived from cluster model calculations, are given in kcal mol^{-1}. For model details see Extended Data Fig. 9.

partial (~30%) transfer of the βd_{xz} electron into the π^* orbital of N_2O through back donation (red orbitals, Fig. 5). Proceeding past the transition state, Mulliken spin analysis on the cluster model indicates that the structure evolves into a transitory $S=5/2$ Fe(III) centre antiferromagnetically coupled to an $N_2O^{\bullet-}$ ligand radical. With further N–O elongation, the α-LUMO (lowest unoccupied molecular orbital) of the $N_2O^{\bullet-}$ ligand radical localizes on the terminal oxygen (blue orbitals, Fig. 5), the N–O bond is cleaved, and N_2 is released. This forms a transient Fe(III)–$O^{\bullet-}$ site with an Fe–O bond of 1.7–1.8 Å, and an O2p_x-derived LUMO. Finally, as the Fe–O bond continues to contract, a second electron is transferred from the Fe centre to its oxyl ligand, resulting in the experimentally defined $S=2$ Fe(IV)=O ground state of α-O. The sequential two-electron reduction of N_2O is calculated to be exothermic by 1.4 kcal mol^{-1} when starting from the O-bound intermediate. It is endothermic by 1.5 kcal mol^{-1} when starting from the N-bound intermediate and exothermic by 6.6 kcal mol^{-1} starting from α-Fe(II) and gas-phase N_2O.

Periodic and cluster model calculations both predict an activation barrier of ~25 kcal mol^{-1} that exceeds the $\Delta H^{\ddagger}=17.7$ kcal mol^{-1} value from experiment. The predicted N–O cleavage barrier correlates strongly with the enthalpic driving force for oxo transfer. We modulated this driving force in cluster models using different hybrid functionals with varying amounts of Hartree Fock exact exchange (compared in Extended Data Fig. 8) and found that the predicted N–O cleavage barrier correlates strongly with the driving force for oxo transfer. The B3LYP functional used here underestimates this driving force, leading to an elevated predicted barrier. However, the electronic structure description of N–O cleavage is robust with respect to the DFT method (that is, functional, periodic versus cluster). Cluster and periodic DFT calculations give comparable O-bound structures and predict similar energetics of N_2O activation in the O-atom reaction coordinate to form α-O. Nevertheless, different lattice topologies and different reactions may exhibit more pronounced confinement or long-range solvation effects than O-atom transfer in *BEA[22], and in those cases periodic and cluster model DFT may give different results.

Correlation of structure to function. As N_2O is a poor σ donor and π acceptor, N_2O-ligated transition metal complexes are rare, and N_2O tends to bind through its terminal N atom. This coordination mode enables backbonding, as the π^* acceptor orbitals of N_2O are polarized toward its terminal N atom[32]. Only a handful of systems that bind N_2O have been experimentally characterized[3–6]. A direct comparison can be made to the metal–organic framework Fe_2(dobdc), with high spin ($S=2$) square pyramidal Fe(II)O_5 centres that bind N_2O as mono-N- and mono-O-bound species in a 60:40 ratio at 10 K. Both binding modes feature long Fe–N_2O distances (2.4 Å) that indicate a lack of backbonding[6]. By contrast, the square planar Fe(II)O_4 centres in Fe-*BEA only form a mono-N-bound species at low temperature, with a Mössbauer quadrupole splitting reflecting backbonding. At room temperature, a much smaller Mössbauer quadrupole splitting is observed, characteristic of a weaker Fe(II)–N_2O interaction with no backbonding. Therefore backbonding is favoured in Fe-*BEA, but not Fe_2(dobdc). A key structural difference between these $S=2$ Fe(II) sites is the presence/absence of an axial ligand. The DFT calculations in Extended Data Fig. 10 indicate that backbonding is decreased by adding an axial ligand to α-N_2O. The axial ligand anchors the Fe centre in the plane of the equatorial ligands, preventing the out-of-plane distortion required to form a short Fe–NNO interaction with backbonding.

Zeolite lattice constraints are known to enforce an 'entatic state' that activates α-O for H-atom abstraction from methane[8,24,33]. Cluster models show that lattice constraints similarly affect the binding and activation of N_2O. In the absence of lattice constraints on the β-6MR ligand, α-Fe(II) is calculated to assume a nearly planar structure (Fig. 6)[34]. For this unconstrained DFT model, N_2O binding through both the O and N atom is enthalpically disfavoured ($\Delta H_{ads}>0$ kcal mol^{-1}). Placing α-Fe(II) in the *BEA lattice constrains the O–Fe–O angle highlighted in yellow in Fig. 6 to 145°, and renders N_2O binding enthalpically favourable. Distortion of the O–Fe–O angle results in a structure resembling a trigonal bipyramidal site with a vacant equatorial position. This destabilizes α-Fe(II) over the five-coordinate N_2O-ligated Fe(II) site and strengthens N_2O binding by 7.1 kcal mol^{-1}, reducing the effective barrier for N_2O activation by 7.7 kcal mol^{-1}.

Formation of α-O from the η^1-O intermediate is the rate-determining step in selective hydrocarbon oxidation[7,27], as well as a critical step in catalytic N_2O decomposition[7]. This study provides an experimentally calibrated reaction coordinate for N_2O activation by an Fe-zeolite. The N–O cleavage on α-Fe(II) in Fe-*BEA can be compared to the activation of N_2O by the binuclear 2Cu(I) active site of Cu-ZSM-5 to form the $[Cu_2O]^{2+}$ reactive intermediate studied in ref. [35]. The experimental apparent barrier for N–O cleavage by Cu-ZSM-5 ($E_a=2.5$ kcal mol^{-1}) is substantially lower than the barrier for Fe-*BEA ($E_a=12.8$ kcal mol^{-1})[35]. To enable quantitative comparison of the electronic structure descriptions of both systems,

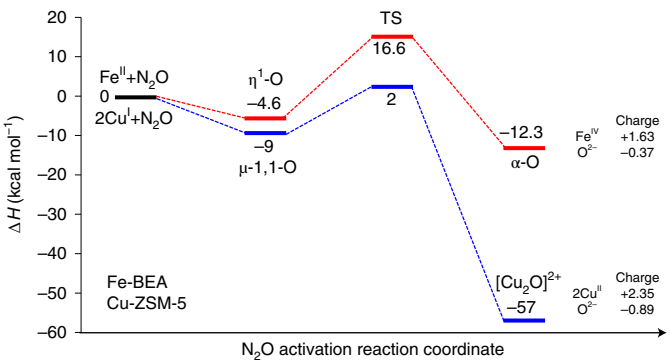

Fig. 7 | DFT reaction profiles for N_2O binding and activation by Cu and Fe zeolites. The profile for the reduced 2Cu(I) active site of Cu-ZSM-5 is shown in blue (values reproduced from ref. [35]). The profile for α-Fe(II) (using the same DFT method as ref. [35] B3LYP without dispersion and using the same basis sets as in the methods of this work) is shown in red. Mulliken charges of the produced metal–oxo complexes are also reported for comparison.

we performed cluster model calculations on Fe-*BEA using the same methodology as in ref. [35] (same basis sets and functional as in the methods of this work, but smaller clusters and no dispersion). The DFT reaction profiles for N_2O activation by Cu-ZSM-5 and Fe-*BEA are compared in Fig. 7. The calculated binding enthalpy of oxygen-bound N_2O in Cu-ZSM-5 (-9 kcal mol^{-1})[35] is about twice that of Fe-*BEA (-4.6 kcal mol^{-1}). This results in a ~4 kcal mol^{-1} reduction of the apparent barrier. The activation barrier for N–O cleavage calculated for Cu-ZSM-5 ($\Delta H^{\ddagger} = 11$ kcal mol^{-1}) is approximately half that of Fe-*BEA ($\Delta H^{\ddagger} = 21.2$ kcal mol^{-1}). The Cu-ZSM-5 reaction is also exothermic by an additional ~40 kcal mol^{-1} due to a large ionic contribution to the product μ-oxo-Cu(II)$_2$ bonds. Correcting for this difference in driving force using Marcus theory[36], the intrinsic barriers for N–O cleavage by Cu-ZSM-5 (30 kcal mol^{-1}) and Fe-*BEA (25 kcal mol^{-1}) are found to be similar. The result is that the more stable $[Cu_2O]^{2+}$ intermediate forms at room temperature, but reacts with methane only at elevated temperatures[37]; while the less stable α-O intermediate forms at elevated temperatures, but reacts with methane at room temperature[7]. The comparison of N_2O activation by α-Fe(II) and this 2Cu(I) site highlights the balancing act between the stability and reactivity of the metal–oxo product.

Conclusions

In this study, we have defined the interaction between N_2O and the α-Fe(II) active site in Fe-*BEA using spectroscopic results coupled to DFT calculations. These data suggest that, at low temperature, an η^1-N species is observed with backbonding from the Fe(II) centre into the N_2O ligand. At room temperature, the Fe(II)–N_2O interaction is weakened, turning off backbonding, and enabling formation of an O-bound intermediate that performs O-atom transfer to Fe(II). Using DR-UV-vis-NIR spectroscopic handles of the α-Fe(II)/α-N_2O/α-O species, we quantified the thermodynamics of N_2O binding and the barrier for N–O bond cleavage. Cluster and periodic DFT calculations provide a unified electronic structure description of the N–O cleavage reaction, where at the transition state ~1/2 of an electron is transferred from the Fe centre into an empty π^* orbital of the N_2O ligand. The close agreement between cluster and periodic calculations, especially with large clusters, indicates that short-range interactions dominate the reaction coordinate in the *BEA lattice. Finally, we have correlated the structure of the Fe(II) active site to its function. We find both Fe(II) out-of-plane distortions due to zeolite lattice constraints and the vacant *trans* axial position tune the thermodynamics of N_2O binding and activation. Comparing Fe(II) and Cu_2(I) active sites in zeolites, we find there is a balance between the driving force for N–O cleavage, and the H-atom abstraction reactivity of the resulting metal–oxo intermediate. Together, these results highlight potential mechanisms for structural control of function in metallozeolite catalysts.

Methods

Sample preparation and treatment. Fe-*BEA (Fe/Al = 0.04; 0.3 wt% Fe) was prepared from calcined (O_2, 823 K) commercial NH_4-beta (*BEA) zeolite (Si/Al = 12.5, CP814E, Zeolyst International) by diffusion impregnation of ^{57}Fe(acac)$_3$ (acac = acetylacetonate) in toluene solution (2.33 mM; 0.25 ml g^{-1} zeolite). The solution was decanted and calcined at 823 K to remove organics. Inductively coupled plasma atomic emission spectroscopy (Perkin Elmer Optima 3300 DV) was performed for elemental analysis. Low iron loadings (0.3 wt%), an organic complex with a protected single iron ion, and the absence of water during preparation were used to ensure a high dispersion of iron and to avoid the formation of oligomers and other spectator species. The sample was pelletized (between 250 and 125 μm), transferred into a quartz tube (~1.5 g of sample) and heated to 1,173 K with a heating ramp of 10 K min^{-1} in a He flow of 20 ml min^{-1}. The sample was kept at 1,173 K for 2 h. Subsequently, the sample was treated in a 20 ml min^{-1} flow of H_2 for 1 h at 973 K, and another hour in a He flow of 20 ml min^{-1} at the same temperature. The H_2 treatment step had only minor effects on the iron speciation. Finally, the sample was cooled to room temperature and either transferred to another quartz sample holder for operando UV-vis spectroscopy or treated in the original piece of quartz glassware for non-operando in situ UV-vis-NIR and Mössbauer spectroscopy. N_2O and He gas flows were controlled with calibrated mass flow controllers (Brooks Instrument 0154) and the temperature was monitored with a thermocouple. Helium flows were oxygen- and moisture-filtered to avoid contamination. Caution was taken to minimize contamination of gas tubing and glassware entrances and exits by air or other contaminants. For reference, a sample was also prepared leaving the Fe(acac)$_3$ out of the preparation.

UV-vis-NIR spectroscopy. Non-operando DR UV-vis-NIR spectra were recorded on a Varian Cary 5000 UV–vis–NIR spectrophotometer at room temperature against a Halon white reflectance standard in the range 4,000–50,000 cm^{-1}.

Operando UV-vis spectroscopy was recorded using an AvaSpec-2048L fibre-optic spectrometer in combination with a DH-2000 deuterium halogen light source (Top Sensor Systems), a FCB-UV400 ME fibre-optic cable and a FCBUV400G-0.1-XHT high-temperature probe. The probe was positioned at a 90° angle to the sample holder (measuring specular reflection). The raw spectra were recorded against a $BaSO_4$ reference. Each spectrum is an average of 49 measurements with an individual integration time of 10.1803 ms.

FTIR spectroscopy. FTIR spectra of N_2O on self-supported zeolite pellets (21.28 mg for Fe-*BEA and 19.82 mg for H-*BEA with an area of 2 cm^2) were recorded using a Nicolet Magna 550-FTIR spectrometer (optical resolution of 4 cm^{-1} and 128 scans) equipped with a mercury cadmium telluride detector. Before adsorption measurements, samples were activated under vacuum (10^{-6} torr) for 5 h at 450 °C and another hour at 550 °C. After cooling, spectra were collected at 77 K. Small doses of N_2O were added into the sample chamber's vacuum by sequentially exposing it to volumes of 2.1 cm^3 containing specified pressures of N_2O at room temperature (see Supplementary Note 2 for more details). During adsorption, the sample was kept at 77 K. Spectra were baselined and analysed using Omnic software (Thermo Fisher).

Mössbauer spectroscopy. The ^{57}Fe Mössbauer spectra were recorded with a See Co.W302 resonant gamma ray spectrometer in horizontal geometry with zero external field using a 1.85-GBq source (Be window, Rh matrix). Data were collected from samples enriched with 100% ^{57}Fe. Isomer shifts are given relative to α-iron metal foil at room temperature (note 'α-iron' here does not refer to the α-Fe(II) site in the zeolite). Spectra were collected with 1,024 points and summed to 512 points before analysing, and then fit with Lorentzian doublets using the Vinda software package for Microsoft Excel.

Calculations with periodic boundary conditions. Static spin–polarized DFT calculations were performed on a periodically extended unit cell of BEA polymorph A[38] containing an α-Fe(II) site in the plane of the six-membered ring and two Al substitutions for charge compensation, positioned as described for the cluster calculations. N_2O adsorption energies were determined using the hybrid B3LYP functional[39,40] with additional Grimme D3 dispersion corrections[41] in a two-level approach. First, a geometry optimization at the PBE-D3 level of theory[42] was carried out using the VASP software package[43–45]. A partial Hessian vibrational analysis was performed on the adsorbate and a 14 T cluster around the acid sites of the optimized structures to verify the true nature of the stationary states and to derive the thermal enthalpy contributions[46,47]. The geometries were further refined by a second optimization at the B3LYP-D3 level of theory using the CP2K software package[48] to obtain more accurate energy estimates. For the N–O cleavage reaction, transition states were localized with the improved dimer method[49,50]. The corresponding reactant and product states were found by following the intrinsic reaction coordinate and minimization via the conjugate gradient algorithm. More details on the computational methodology are provided in the Supplementary Methods.

Infrared vibrations and Mössbauer parameters were calculated by methods described under the cluster calculations on cluster models cut out of the periodically geometry optimized models. The geometry optimized cutouts comprised the 6MR extended with one T site. These were then capped with hydrides.

Cluster model calculations. Cluster models were generated from crystallographic coordinates of BEA polymorph A, as outlined in refs. [8,24], but with capping hydrides at 1.42 Å instead of capping hydroxyls to reduce computation times (see Supplementary Data for the coordinates). To model α-Fe(II), two Si atoms in a β-type six-membered ring were substituted for Al atoms. This Al configuration was shown to be representative for α-Fe(II) in the different (experimentally indistinguishable) β-type exchange sites found in *BEA polymorphs A and B[24]. Unless specified otherwise, spin-unrestricted DFT calculations were performed with Gaussian 09 (revision D.01)[51] using the B3LYP functional with the D3 dispersion correction of Grimme[41]. The 6-311G* basis set was used for Fe, for atoms directly coordinated to Fe and for N_2O. The 6-31G* basis set was used for all other atoms. For geometry optimizations, the six T sites of the β-6MR ligand were allowed to relax, and all other atoms were frozen at their crystallographic positions. Enthalpy changes were derived from single point calculations performed on optimized structures, but using a larger basis (6-311 + G* on Fe, coordinating atoms and N_2O; 6-311G* on all others). Thermal contributions to the enthalpy were calculated from vibrational analysis on optimized structures. For the N–O

cleavage reaction coordinates, the N–O cleavage transition state was verified to contain a single imaginary frequency corresponding to motion along the reaction coordinate.

Mössbauer quadrupole splittings were calculated using the B3LYP functional, with the TZVP basis set on Fe and coordinating O atoms and 6-31G* on all other atoms. Isomer shifts were calculated with the ORCA computational package (version 303)[52] using the B3LYP functional. The CP(PPP) basis set[53] was used on Fe, with 6-311G* on coordinating O atoms and 6-31G* on all others. A calibration curve was generated by relating the DFT-calculated electron densities at the iron nucleus ($|\psi_0|^2$) to the experimental isomer shifts for a test set of 23 structurally defined Fe complexes. The isomer shift values were then estimated from the value of $|\psi_0|^2$ calculated for each cluster model.

Data availability

Additional data are available in the Supplementary Methods and Supplementary Data. Any unavailable data that support the findings of this study can be requested from the authors. See the author contributions for specific datasets.

Received: 16 August 2018; Accepted: 12 March 2021;
Published online: 22 April 2021

References

1. *IPCC Climate Change 2013: The Physical Science Basis* (eds Stocker, T. F. et al.) (Cambridge Univ.Press, 2013).
2. Tolman, W. B. Binding and activation of N_2O at transition-metal centers: recent mechanistic insights. *Angew. Chem. Int. Ed.* **49**, 1018–1024 (2010).
3. Paulat, F. et al. Spectroscopic properties and electronic structure of pentammineruthenium(II) dinitrogen oxide and corresponding nitrosyl complexes: binding mode of N_2O and reactivity. *Inorg. Chem.* **43**, 6979–6994 (2004).
4. Pamplin, C.B., Ma, E.S. F., Safari, N., Rettig, S.J. & James, B.R. The nitrous oxide complex, $RuCl_2(\eta1\text{-}N_2O)$(P-N)($PPh_3$) (P-N = [*o*-(*N*,*N*-dimethylamino) phenyl]diphenylphosphine); low temperature conversion of N_2O to N_2 and O_2. *J. Am. Chem.Soc.* **123**, 8596–8597 (2001).
5. Piro, N. A., Lichterman, M. F., Harman, W. H. & Chang, C. J. A structurally characterized nitrous oxide complex of vanadium. *J. Am. Chem. Soc.* **133**, 2108–2111 (2011).
6. Xiao, D. J. et al. Oxidation of ethane to ethanol by N_2O in a metal–organic framework with coordinatively unsaturated iron(II) sites. *Nat. Chem.* **6**, 590–595 (2014).
7. Panov, G. I., Sobolev, V. I. & Kharitonov, A. S. The role of iron in N_2O decomposition on ZSM-5 zeolite and reactivity of the surface oxygen formed. *J. Mol. Catal.* **61**, 85–97 (1990).
8. Snyder, B. E. R. et al. The active site of low-temperature methane hydroxylation in iron-containing zeolites. *Nature* **536**, 317–321 (2016).
9. Kondratenko, E. V. & Pérez-Ramírez, J. Mechanism and kinetics of direct N_2O decomposition over Fe-MFI zeolites with different iron speciation from temporal analysis of products. *J. Phys. Chem. B* **110**, 22586–22595 (2006).
10. Zecchina, A., Rivallan, M., Berlier, G., Lamberti, C. & Ricchiardi, G. Structure and nuclearity of active sites in Fe-zeolites: comparison with iron sites in enzymes and homogeneous catalysts. *Phys. Chem. Chem. Phys.* **9**, 3483–3499 (2007).
11. Liu, N. et al. Charge transfer analysis on the direct decomposition of nitrous oxide over Fe-BEA zeolite: an experimental and density functional study. *J. Phys. Chem. C* **115**, 12883–12890 (2011).
12. Chen, B. et al. Study on the direct decomposition of nitrous oxide over Fe-beta zeolites: from experiment to theory. *Catal. Today* **175**, 245–255 (2011).
13. Berlier, G. et al. Evolution of extraframework iron species in Fe silicalite. *J. Catal.* **208**, 64–82 (2002).
14. Rivallan, M., Ricchiardi, G., Bordiga, S. & Zecchina, A. Adsorption and reactivity of nitrogen oxides (NO_2, NO, N_2O) on Fe-zeolites. *J. Catal.* **264**, 104–116 (2009).
15. Wood, B. R., Reimer, J. A. & Bell, A. T. Studies of N_2O adsorption and decomposition on Fe-ZSM-5. *J. Catal.* **209**, 151–158 (2002).
16. Wang, Y., Lei, Z., Chen, B., Guo, Q. & Liu, N. Adsorption of NO and N_2O on Fe-BEA and H-BEA zeolites. *Appl. Surf. Sci.* **256**, 4042–4047 (2010).
17. Krebs, C., Fujimori, D. G., Walsh, C. T. & Bollinger, J. M. Non-heme Fe(IV)-oxo intermediates. *Acc. Chem. Res.* **40**, 484–492 (2007).
18. Price, J. C., Barr, E. W., Tirupati, B., Bollinger, J. M. & Krebs, C. The first direct characterization of a high-valent iron intermediate in the reaction of an α-ketoglutarate-dependent dioxygenase: a high-spin Fe(IV) complex in taurine/α-ketoglutarate dioxygenase (TauD) from *Escherichia coli*. *Biochemistry* **42**, 7497–7508 (2003).
19. Eckhause, M., Harris, R. J., Shuler, W. B. & Welsh, R. E. A measurement of the lifetime of the 14.4-kev level of ^{57}Fe. *Proc. Phys. Soc.* **89**, 187–188 (1966).
20. Brozek, C. K., Ozarowski, A., Stoian, S. A. & Dincă, M. Dynamic structural flexibility of Fe-MOF-5 evidenced by ^{57}Fe Mössbauer spectroscopy. *Inorg. Chem. Front.* **4**, 782–788 (2017).
21. Shimanouchi, T. Tables of molecular vibrational frequencies. Consolidated volume II. *J. Phys. Chem. Ref. Data* **6**, 993–1102 (1977).
22. Göltl, F. et al. Computationally exploring confinement effects in the methane-to-methanol conversion over iron–oxo centers in zeolites. *ACS Catal.* **6**, 8404–8409 (2016).
23. Snyder, B. E. R., Vanelderen, P., Schoonheydt, R. A., Sels, B. F. & Solomon, E. I. Second-sphere effects on methane hydroxylation in Cu-zeolites. *J. Am. Chem. Soc.* **140**, 9236–9243 (2018).
24. Snyder, B. E. R. et al. Structural characterization of a non-heme iron active site in zeolites that hydroxylates methane. *Proc. Natl Acad. Sci. USA* **115**, 4565–4570 (2018).
25. Bols, M. L. et al. Spectroscopic identification of the α-Fe/α-O active site in Fe-CHA zeolite for the low-temperature activation of the methane C–H bond. *J. Am. Chem. Soc.* **140**, 12021–12032 (2018).
26. Clark, M. G., Bancroft, G. M. & Stone, A. J. Mössbauer spectrum of Fe^{2+} in a square-planar environment. *J. Chem. Phys.* **47**, 4250–4261 (1967).
27. Panov, G. I., Sheveleva, G. A., Kharitonov, A. S., Romannikov, V. N. & Vostrikova, L. A. Oxidation of benzene to phenol by nitrous oxide over Fe-ZSM-5 zeolites. *Appl. Catal. A Gen.* **82**, 31–36 (1992).
28. Sobolev, V. I. et al. Catalytic properties of ZSM-5 zeolites in N_2O decomposition: the role of iron. *J. Catal.* **139**, 435–443 (1993).
29. Kiwi-Minsker, L., Bulushev, D. A. & Renken, A. Low temperature decomposition of nitrous oxide over Fe/ZSM-5: modelling of the dynamic behaviour. *Catal. Today* **110**, 191–198 (2005).
30. Wood, B. R., Reimer, J. A., Bell, A. T., Janicke, M. T. & Ott, K. C. Nitrous oxide decomposition and surface oxygen formation on Fe-ZSM-5. *J. Catal.* **224**, 148–155 (2004).
31. Pidko, E. A. Toward the balance between the reductionist and systems approaches in computational catalysis: model versus method accuracy for the description of catalytic systems. *ACS Catal.* **7**, 4230–4234 (2017).
32. Tolman, W. B. Binding and activation of N_2O at transition-metal centers: recent mechanistic insights. *Angew. Chem. Int. Ed.* **49**, 1018–1024 (2010).
33. Snyder, B. E. R., Bols, M. L., Schoonheydt, R. A., Sels, B. F. & Solomon, E. I. Iron and copper active sites in zeolites and their correlation to metalloenzymes. *Chem. Rev.* **118**, 2718–2768 (2018).
34. Hallaert, S. D. et al. Identification of α-Fe in high-silica zeolites on the basis of ab initio electronic structure calculations. *Inorg. Chem.* **56**, 10681–10690 (2017).
35. Tsai, M. L. et al. $[Cu_2O]^{2+}$ active site formation in Cu-ZSM-5: geometric and electronic structure requirements for N_2O activation. *J. Am. Chem. Soc.* **136**, 3522–3529 (2014).
36. Marcus, R. A. Theoretical relations among rate constants, barriers, and Brønsted slopes of chemical reactions. *J. Phys. Chem.* **72**, 891–899 (1968).
37. Woertink, J. S. et al. A $[Cu_2O]^{2+}$ core in Cu-ZSM-5, the active site in the oxidation of methane to methanol. *Proc. Natl Acad. Sci. USA* **106**, 18908–18913 (2009).
38. Baerlocher, C. & McCusker, L. B. *Database of Zeolite Structures* (IZA-SC, accessed 25 April 2017); http://www.iza-structure.org/databases/
39. Becke, A. D. Density-functional exchange-energy approximation with correct asymptotic behavior. *Phys. Rev. A* **38**, 3098–3100 (1988).
40. Lee, C., Yang, W. & Parr, R. G. Development of the Colle–Salvetti correlation-energy formula into a functional of the electron density. *Phys. Rev. B* **37**, 785–789 (1988).
41. Grimme, S., Antony, J., Ehrlich, S. & Krieg, H. A consistent and accurate ab initio parametrization of density functional dispersion correction (DFT-D) for the 94 elements H–Pu. *J. Chem. Phys.* **132**, 154104 (2010).
42. Perdew, J. P., Burke, K. & Ernzerhof, M. Generalized gradient approximation made simple. *Phys. Rev. Lett.* **77**, 3865–3868 (1996).
43. Kresse, G. & Hafner, J. Ab initio molecular dynamics for liquid metals. *Phys. Rev. B* **47**, 558–561 (1993).
44. Kresse, G. & Hafner, J. Ab initio molecular-dynamics simulation of the liquid-metalamorphous-semiconductor transition in germanium. *Phys. Rev. B* **49**, 14251–14269 (1994).
45. Kresse, G. & Furthmüller, J. Efficient iterative schemes for ab initio total-energy calculations using a plane-wave basis set. *Phys. Rev. B* **54**, 11169–11186 (1996).
46. Van Speybroeck, V. et al. Advances in theory and their application within the field of zeolite chemistry. *Chem. Soc. Rev.* **44**, 7044–7111 (2015).
47. Ghysels, A., Verstraelen, T., Hemelsoet, K., Waroquier, M. & Van Speybroeck, V. TAMkin: a versatile package for vibrational analysis and chemical kinetics. *J. Chem. Inf. Model.* **50**, 1736–1750 (2010).
48. Vandevondele, J. et al. Quickstep: fast and accurate density functional calculations using a mixed Gaussian and plane waves approach. *Comput. Phys. Commun.* **167**, 103–128 (2005).
49. Heyden, A., Bell, A. T. & Keil, F. J. Efficient methods for finding transition states in chemical reactions: comparison of improved dimer method and partitioned rational function optimization method. In *AIChE Annual Meeting, Conference Proceedings* Vol. 123, 11531 (American Institute of Physics, 2005).

50. Henkelman, G. & Jónsson, H. Improved tangent estimate in the nudged elastic band method for finding minimum energy paths and saddle points. *J. Chem. Phys.* **113**, 9978–9985 (2000).
51. Frisch, M. J. et al. Gaussian 09, Revision D.01 (Gaussian, 2009).
52. Neese, F. The ORCA program system. *WIREs Comput. Mol. Sci.* **2**, 73–78 (2012).
53. Neese, F. Prediction and interpretation of the ^{57}Fe isomer shift in Mössbauer spectra by density functional theory. *Inorg. Chim. Acta* **337**, 181–192 (2002).

Acknowledgements

This investigation has been supported by the Flemish Science Foundation (FWO, grant no. G0A2216N to B.F.S. and R.A.S.) and the National Science Foundation (grant no. CHE-1660611 to E.I.S.). B.E.R.S. acknowledges support from the National Science Foundation Graduate Research Fellowship Program under grant no. DGE-11474 and from the Munger, Pollock, Reynolds, Robinson, Smith & Yoedicke Stanford Graduate Fellowship. M.L.B. acknowledges the Research Foundation–Flanders for funding of his stay at Stanford University (grant no. V417018N). E.I.S. acknowledges support from the Stanford Woods Institute for the Environment. P.C. and V.V.S. acknowledge the Research Board of Ghent University (BOF) and funding from the European Union's Horizon 2020 research and innovation programme (consolidator ERC grant agreement no. 647755–DYNPOR (2015–2020)). The work by G.W. was supported by the ANR-Total 'Nanoclean Energy' chair and Normandy's RIN program. The computational resources and services for the periodic calculations were provided by Ghent University (Stevin Supercomputer Infrastructure) and the VSC (Flemish Supercomputer Centre), funded by the Research Foundation–Flanders (FWO).

Author contributions

M.L.B., B.E.R.S., B.F.S., E.I.S. and R.A.S. designed the experiments. M.L.B., B.E.R.S. and H.M.R. performed the experiments. G.F. performed the FTIR experiments. B.E.R.S. performed the cluster DFT calculations. P.C. and V.V.S. performed the periodic DFT calculations. M.L.B., B.E.R.S., H.M.R., P.C., V.V.S., B.F.S. and E.I.S. analysed the data. M.L.B., B.E.R.S. and H.M.R. wrote the manuscript with guidance from R.A.S., E.I.S. and B.F.S.

Competing interests

The authors declare no competing interests.

Additional information

Extended data is available for this paper at https://doi.org/10.1038/s41929-021-00602-4.

Supplementary information The online version contains supplementary material available at https://doi.org/10.1038/s41929-021-00602-4.

Correspondence and requests for materials should be addressed to R.A.S., V.V.S., E.I.S. or B.F.S.

Peer review information *Nature Catalysis* thanks Dennis Palagin and the other, anonymous, reviewer(s) for their contribution to the peer review of this work.

Reprints and permissions information is available at www.nature.com/reprints.

Publisher's note Springer Nature remains neutral with regard to jurisdictional claims in published maps and institutional affiliations.

© The Author(s), under exclusive licence to Springer Nature Limited 2021

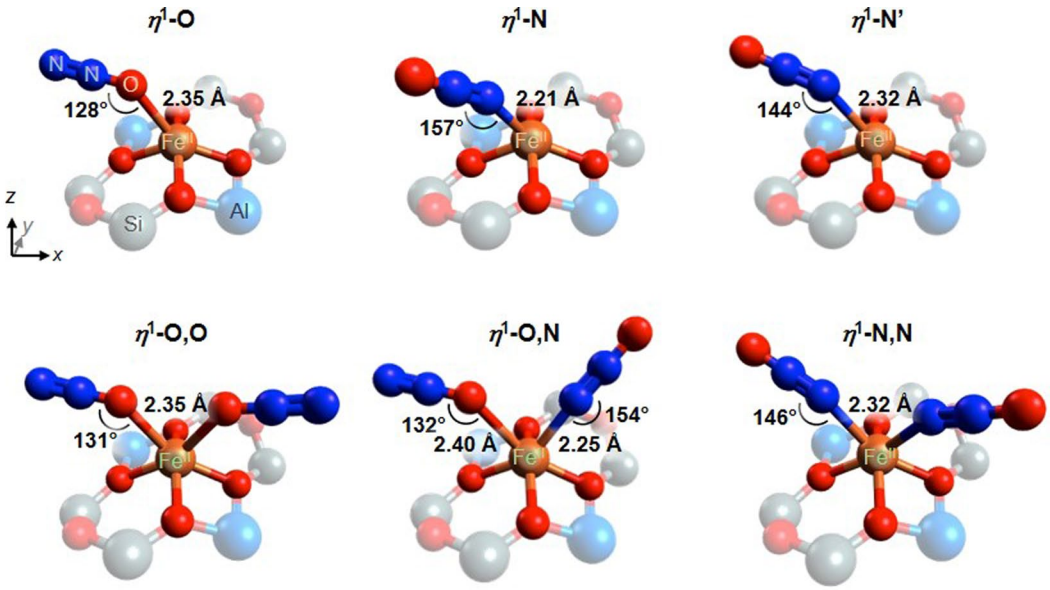

	η^1-O	η^1-N	η^1-N'	η^1-O,O	η^1-O,N	η^1-N,N
$\Delta H_{ads,298K}$ (kcal/mol)	-4.4	-3.9	-3.5	-8.3	-7.9	-6.2
ZPE corrected $\Delta E_{el,ads}$	-4.3	-3.6	-3.4	-8.1	-7.6	-5.9
LF band (cm^{-1})	12300	6300	11600	10400 6100	6500	none
ΔE_Q (mm/s)	-1.63	2.39	-1.76	2.50	3.02	4.15
ν_{as} (cm^{-1})	2382	2412	2392	2385	2387, 2411	2401
ν_s (cm^{-1})	1284	1393	1389	1292	1294, 1389	1385
β HOMO	d_{z^2}	d_{xz}	d_{z^2}	d_{z^2}/d_{xz}	d_{z^2}/d_{xz}	d_{xy}

Extended Data Fig. 1 | Comparison of the six possible N_2O-bound models. The models are evaluated by cluster DFT calculations. It is not possible to bind additional N_2O ligands to the sterically protected *trans* axial positions of these sites. In the table, the predicted properties of these models are compared. DFT calculations predict S = 2 ground states for all six models. Based on their predicted quadrupole splittings, the η^1-O,O/η^1-O,N models are potential structural models of the α-$(N_2O)_2$ LT2 species observed at low temperature and high N_2O concentrations (see Fig. 1f). Values of $\Delta H_{ads,298K}$ and $\Delta E_{el,ads}$ in this figure are relative to lattice adsorbed N_2O.

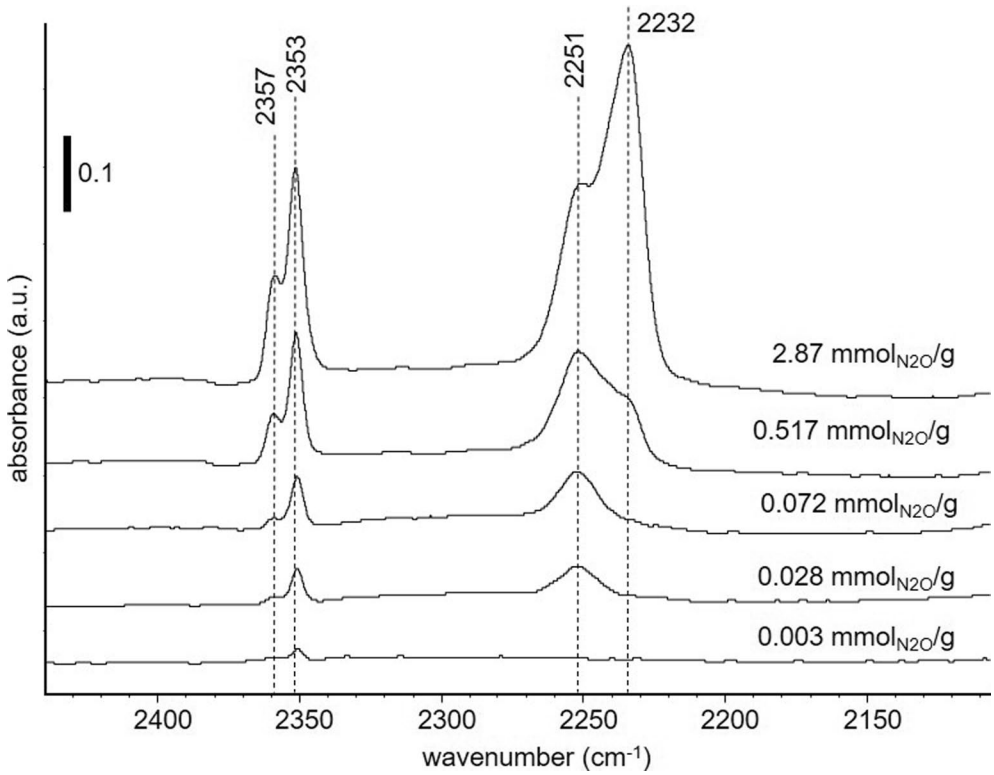

Extended Data Fig. 2 | FTIR spectra of different amounts of N_2O loaded onto H-*BEA at 77 K. The antisymmetric N_2O stretch region measured at 77 K through FTIR on H-*BEA in vacuum that is cumulatively loaded with pulses of N_2O from the gas phase at 77 K.

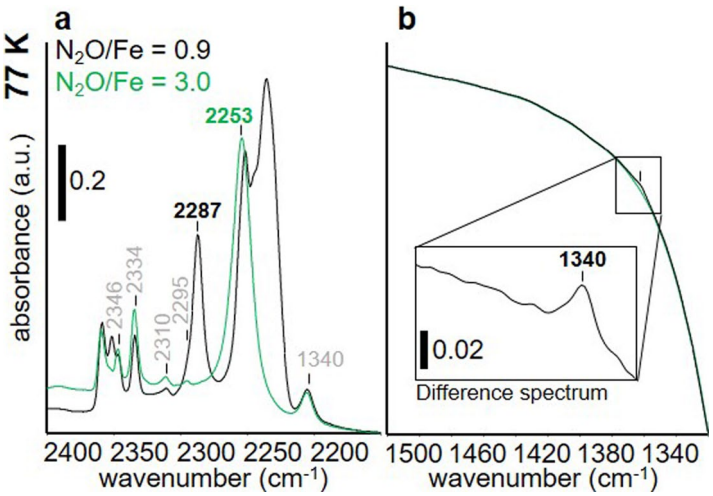

Extended Data Fig. 3 | FTIR spectra at 77K of Fe-*BEA loaded with 0.9 N_2O/Fe and 3.0 N_2O/Fe. a) antisymmetric stretching region, **b)** symmetric stretching region.

A. η^1-N	d(Fe-N) (Å)	β homo	ΔE_Q (mm/s)	ΔE_{ads} (kcal/mol)
T4/T4'	2.12	d_{xz}	+2.22	-10.1
T6/T6'	2.21	d_{xz}	+2.39	-3.9
T8/T8'	2.14	d_{xz}	+2.30	-11.5

B. η^1-O	d(Fe-O) (Å)	β homo	ΔE_Q (mm/s)	ΔE_{ads} (kcal/mol)
T4/T4'	2.22	$d_{z^2}/d_{x^2-y^2}$	+2.45	-8.1
T6/T6'	2.35	d_{z^2}	-1.63	-3.9
T8/T8'	2.22	$d_{z^2}/d_{x^2-y^2}$	+2.11	-9.4

C. TS	d(Fe-O) (Å)	d(Fe-N) (Å)	$Q_{TS}(N_2O)$	ΔE_{act} (kcal/mol)
T4/T4'	1.81	1.50	-0.26	27.4
T6/T6'	1.83	1.46	-0.29	27.9
T8/T8'	1.80	1.54	-0.22	30.9

D. η^1-O	d(Fe-ONN) (Å)	$d(Fe\text{-}O)_{avg}$ (Å)	$<O\text{-}Fe\text{-}O_{avg}$	<Fe-O-NN
T4/T4'	2.22	2.07	144°	135°
T7/T7'	2.21	2.08	146°	137°
T6/T6'	2.35	2.03	147°	128°
T5/T5'	2.35	2.03	148°	128°
T8/T8'	2.22	2.08	140°	140°
T3/T3'	2.22	2.08	142°	141°

Extended Data Fig. 4 | Parameters for different aluminium substitutions in cluster models. a) η^1-N models, **b)** η^1-O models, **c)** Transition state models. The associated ZPE corrected electronic energies of N_2O adsorption and activation included at the right of each table. $Q_{TS}(N_2O)$ quantifies the extent of charge transfer from the Fe centre into the N_2O ligand at the N-O cleavage transition state. Note that the results of the T3/T3′, T5/T5′, and T7/T7′ sites parallel those of the T4/T4′, T6/T6′, and T8/T8′ sites, respectively. A comparison of this is shown in **d)**. Reference level is N_2O bound to the zeolite lattice.

	d(Fe-O) (Å)	d(O-N) (Å)	<(Fe-O-N) (°)	$\Delta E_{el,B3LYP-D3}$ (kcal/mol)	$\Delta H_{298K,B3LYP-D3}$ (kcal/mol)
N_2O adsorbed to the lattice without Fe*				-5.4	-4.6
η^1-N bound				-13.4	-12.9
η^1-O bound				-10.5	-9.8
Reactant	2.27	1.21	142	-9.1	-8.6
TS	1.82	1.56	135	16.0	15.1
Product	1.61	3.03	133	-12.5	-11.2

Extended Data Fig. 5 | B3LYP-D3 optimized models in CP2K. Data given are Fe-ON_2 and O-N_2 bond distances, Fe-O-N_2 bond angle, electronic energies, and adsorption enthalpies at 298K (with respect to the empty Fe-BEA framework and N_2O in gas phase) of the transition state and corresponding reactant and product minima for the N-O cleavage reaction in Fe-BEA, obtained from the geometry optimisations at the B3LYP-D3 level of theory in CP2K. * N_2O adsorbed to the lattice without Fe is used as the reference level in the main manuscript, that is −5.4 kcal/mol is subtracted from the $\Delta E_{el,B3LYP-D3}$ values and −4.6 kcal/mol is substracted from the $\Delta H_{298K,B3LYP-D3}$ values.

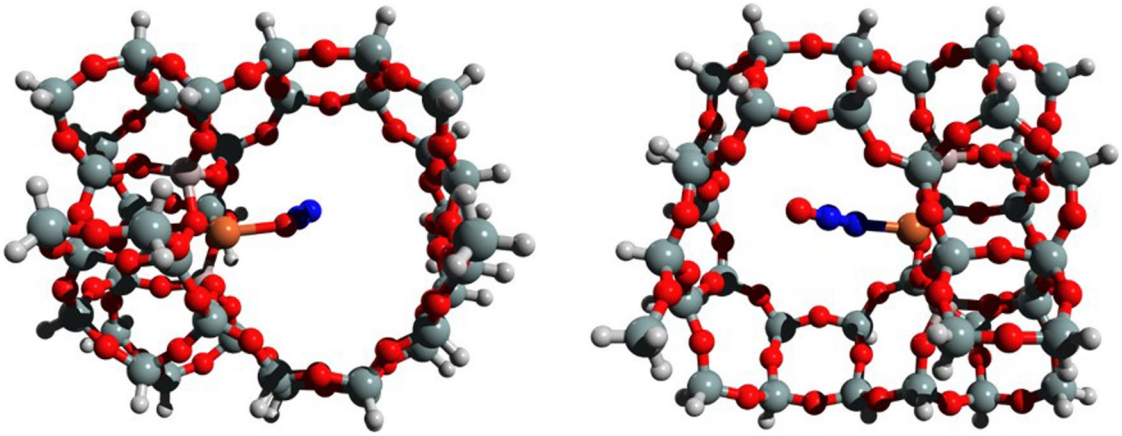

	$\Delta H_{ads,298K,B3LYP-D3}(\eta^1\text{-O bound}) - \Delta H_{ads,298K,B3LYP-D3}(\eta^1\text{-N bound})$ (kcal/mol)
Regular cluster models	-0.5
large cluster models	3.5
Periodic calculations	3.1

Extended Data Fig. 6 | Large structure optimised cluster models of η^1-O bound and η^1-N bound. The same functionals and methods were used as for the smaller cluster models, as described in the methods section. The table shows difference in enthalpy between η^1-O bound and η^1-N bound using different methods.

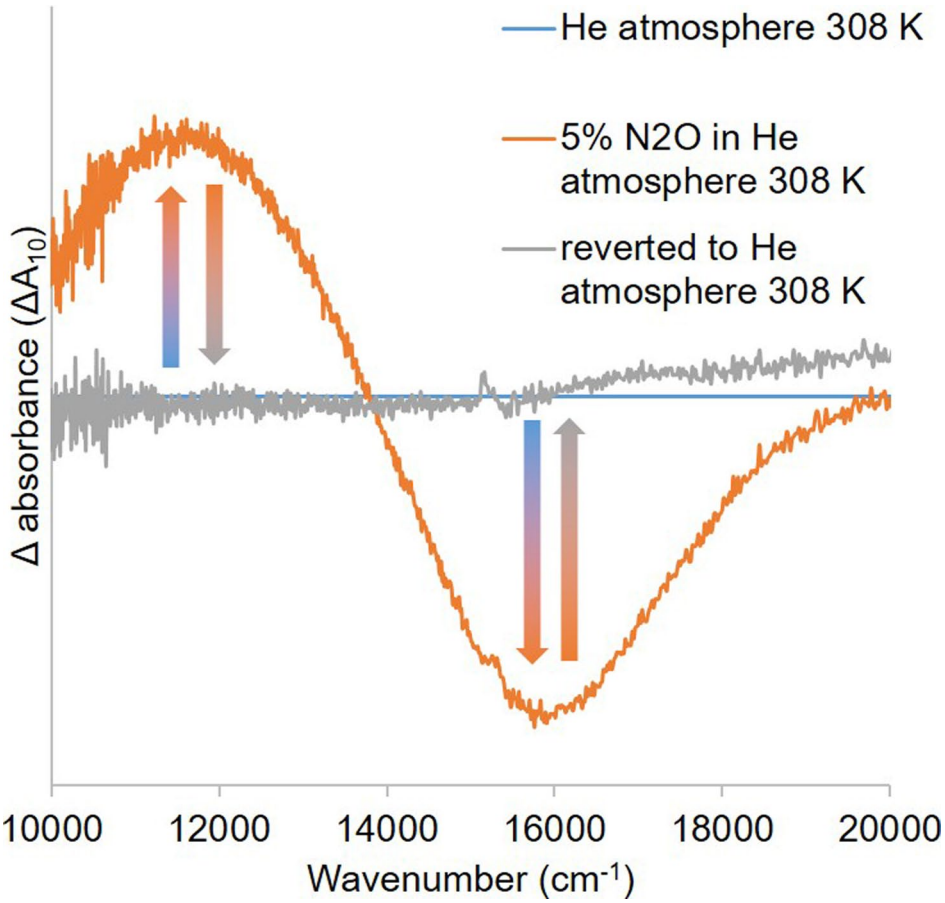

Extended Data Fig. 7 | Difference UV-Vis spectra upon N_2O exposure. Spectra are relative to the spectrum of Fe(II)-*BEA after He 1,173 K before introduction of a 35 vol.% N_2O atmosphere (blue). The orange spectrum is after introduction of the N_2O atmosphere, the grey spectrum after subsequent removal of the N_2O atmosphere at 308 K.

functional	η^1-O	N-O TS	α-O	intrinsic barrier
B3P86 with 30% HF exchange	0	31.2	7.7	27.2
B3LYP with 20% HF exchange	0	23.8	-6.4	26.9
B3P86 with 15% HF exchange	0	13.3	-24.4	24.0

Extended Data Fig. 8 | Effect of Hartree-Fock exchange on the predicted energetics of the N-O cleavage reaction. ΔE values are given in kcal/mol. The three functionals predict different driving forces for O-atom transfer, but similar intrinsic barriers. The intrinsic barriers are calculated by using a Marcus Theory correction. These calculations were done without dispersion or single point calculations on a higher basis set and cannot be directly compared to the data in Figs 5 and 6.

	ZPE corrected $\Delta E_{el,B3LYP-D3}$ (kcal/mol)	$\Delta H_{298K,B3LYP-D3}$ (kcal/mol)
α-Fe(II) + N_2O adsorbed to the empty lattice	0.0	0.0
η^1-O bound	2.8	2.7
TS	29.5	29.1

Extended Data Fig. 9 | Unconstrained toy model energies and enthalpies used in figure 6. Energies are relative to α-Fe(II) + N_2 coordinated to lattice. The size of the unconstrained model is a 6MR capped with hydrides. Calculations on the unconstrained model were with dispersion and larger basis set single point calculation as described in the methods.

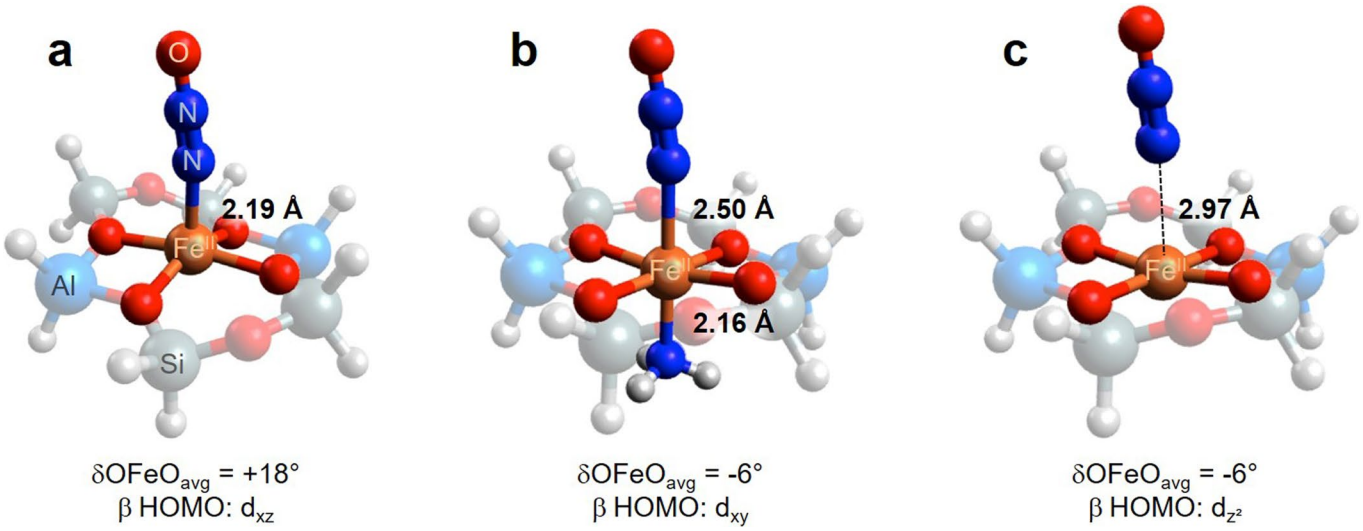

Extended Data Fig. 10 | Small cluster models evaluating the effect of a trans-axial ligand. a) toy model of the N-bound Fe^{II} species, in which the 6-membered ring ligand is capped with hydrogens and allowed to freely geometry optimise, **b)** geometry optimised structure including an axial amine ligand, and **c)** structure in which the axial amine ligand is deleted, and the coordinates of the N_2O ligand are re-optimised (that is the Fe^{II} and 6-membered ring ligand are frozen). For each model, the out-of-plane distortion of the iron atom is quantified by the average distortion of the O-Fe-O angle ($\delta OFeO_{avg}$), and the doubly-occupied orbital is indicated.